Progress in Natural Science: Materials International 36 (2026) 175–186

HOSTED BY

Contents lists available at ScienceDirect

Progress in Natural Science: Materials International

journal homepage: www.elsevier.com/locate/pnsmi

Zwitterion-enhanced polarization loss in Magnetic ionic liquid/CNT composite gel for broadband electromagnetic wave absorption

Chenjian Li[a,1], Wenlai Xia[b,1], Dangfeng Zhou[a], Gang Lu[a], Hongmei Qin[b], Shixian Zhang[c], Xueliang Jiang[a,*], Chuanxi Xiong[b,**]

[a] Hubei Key Laboratory of Plasma Chemistry and Advanced Materials, School of Materials Science and Engineering, Wuhan Institute of Technology, Wuhan, 430205, China
[b] State Key Laboratory of Silicate Materials for Architectures, School of Materials Science and Engineering, Wuhan University of Technology, 430070, Wuhan, China
[c] Department of Materials Science and Engineering, The Pennsylvania State University, PA, USA

ARTICLE INFO

Keywords:
Carbon nanotube
Effective absorption band
Impedance match
Magnetic ionic liquid
Zwitterion

ABSTRACT

The composites composed of Carbon nanotube (CNT) and inorganic magnetic materials are candidates for broadband electromagnetic wave (EMW) absorbing materials (EWAM). However, poor interfacial compatibility between CNT and inorganic magnetic materials limits the enhancement of broadband EMW absorption performance. Herein, this study innovatively prepared the organic magnetic ionic liquid (MIL) with a zwitterionic structure and combined it with CNT to obtain the "Magnetic ionic liquid/CNT composite gel" (MIL/CNT). In the MIL/CNT, the energy of EMW is well attenuated through the multi-EMW dissipating routes, such as conductance loss, polarization loss and magnetic loss. Remarkably, attributed to the zwitterionic structure, the stronger ionic dipole polarization loss has been induced to dissipate the EMW, which achieved an effective absorption band (EAB) of 7.5 GHz (9.44–16.94 GHz) and minimum reflection loss (RL_{min}) of −46 dB with 2.1 mm thickness at 15.8 GHz. The MIL/CNT composite demonstrated excellent broadband electromagnetic wave absorption, offering a novel strategy for fabricating EMW defense materials with a wide operational frequency range.

1. Introduction

With the development of communication and radar technology, multi-frequency range electromagnetic waves (EMW) have been applied, however, they also induce serious electromagnetic interference. Thus, achieving broadband electromagnetic wave absorption is a major challenge in developing high-performance EWAM [1–3]. Relying on a single electromagnetic dissipation mechanism inevitably leads to insufficient performance, making it difficult to fulfill the aforementioned demands. Therefore, compound EWAM with multiple dissipating routes gradually becomes the EMW development direction of EWAM.

The carbon nanotube (CNT) is an excellent candidate for EWAM due to its low density, high specific surface area and excellent electrical conductivity [4–7]. Unfortunately, poor impedance matching of CNT caused by excessively high electrical conductivity leads to strong reflection of EMW. Meanwhile, the single monotonic dielectric loss route of CNT is negative for EMW attenuation at multi-band frequencies. Thus, CNT used alone as EWAM hardly achieves satisfactory broadband EMW absorbing performance [8,9]. Nevertheless, combining the inorganic nano-magnetic materials with CNT, such as magnetic ferrite and magnetic metal powder, can effectively enhance the effective absorption band (EAB) through inducing the magnetic loss [8–13]. However, the poor interfacial compatibility between CNT and inorganic magnetic materials resulted in agglomeration, which is negative for wide frequency EMW absorbing properties [14,15].

Recently, many reports have improved the compatibility between CNT and inorganic magnetic materials. Our team reported a solvent-free fluid Fe_3O_4 (S-Fe_3O_4) with an organic long-chain bilayer and S-Fe_3O_4/CNT composites. The organic long chain in S-Fe_3O_4 can well modified the interfacial compatibility between CNT and promote the uniform dispersion of CNT. Thus, the S-Fe_3O_4/CNT composites achieved 5.2 GHz of EAB [15]. Referring to the above work, the magnetic ionic liquids (MIL) formed by imidazolium salts complexed with transition metal ions [16–18], which have chemical and thermal stability. The MIL exhibits

* Corresponding author. No. 206, Guanggu 1st Road, Wuhan, 430205, China.
** Corresponding author. No. 205, Luoshi Road, Wuhan, 430070, Hubei, China.
E-mail addresses: jiangxl@wit.edu.cn (X. Jiang), cxiong@whut.edu.cn (C. Xiong).
[1] These authors contributed equally to this work.

https://doi.org/10.1016/j.pnsc.2026.01.005
Received 14 October 2025; Received in revised form 7 January 2026; Accepted 15 January 2026
Available online 9 February 2026

favorable compatibility and bendability with CNT due to the cation-π interaction between them [19]. Thus, the MIL can be combined with CNT to form gel-like composites, which are called "Bucky gel" [20]. In the MIL/CNT composites, the MIL not only can optimize the dielectric constants of CNT, approach the impedance of free space, reducing EMW reflection, but also can attenuate the energy of EMW through conduction loss, ionic dipole polarization loss and magnetic loss from the unique metal ionic group [21–24].

In this paper, the classical magnetic ionic liquid, 1-Butyl-3-methylimidazolium Tetrachloroferrate (Bmim[$FeCl_4$]), was synthesized via the complexing reaction between butyl-3-methylimidazolium chloride ([Bmim]Cl) and $FeCl_3$. Simultaneously combined with CNT to obtain the gel-like composite, the Bmim[$FeCl_4$]/CNT. Moreover, the zwitterion, 1-propyl sulfonic-3-methylimidazolium ($PIMSO_3$), and [Bmim]Cl together complexed with $FeCl_3$ to form the zwitterionic MIL ($PIMSO_3$Bim[$FeCl_4$]), which enhances the combination between MIL and CNT through ion-dipole or dipole-dipole interaction [19,20]. More interestingly, the zwitterion induced stronger ionic dipole polarization loss. Thus, besides the magnetism loss, a stronger dipole polarization occurred in $PIMSO_3$Bim[$FeCl_4$]/CNT than Bmim[$FeCl_4$]/CNT, while optimizing the impedance matching, thereby achieving a broadband EMW absorption performance. The Vector network analyzer (VNA), spectrum and electron microscope technology, respectively, revealed the EMW absorption performance and underlying EMW dissipating mechanism of MIL/CNT.

2. Experiment section

2.1. Materials

CNTs were purchased from Chengdu Organic Chemicals Co., Ltd (diameter: 5–15 nm, length: 50 μm and purity is 95 %). Other analytical grade chemicals, the imidazolium salts, 1-propyl sulfonic-3-methylimidazolium ($PIMSO_3$) and 1-butyl-3-methylimidazolium chloride ([Bmim]Cl) were supported by Shanghai Chengjie Chemical Co., LTD. The pure chemicals, including methanols, were purchased from Sino Pharm Chemical Reagent Co., Ltd. All chemicals were directly used without purification.

2.2. Fabrication of MIL/CNT

The preparation processes for various "Magnetic ionic liquid/CNT composite gels" are illustrated in Fig. 1. The $PIMSO_3$, [Bmim]Cl and the mixture of $PIMSO_3$ and [Bmim]Cl were mixed with CNT in a 50 mL methanol in flask, respectively, and then sonicated for 1 h to form the dispersion. Nitrogen (N_2) was passed through the above dispersion for 20 min to displace the air. Subsequently, the $FeCl_3$ was quickly added to the dispersion and complexed with the imidazolium salt in methanol at 40 °C with magnetic stirring for 5h. Finally, various MIL/CNT, the $PIMSO_3$Bim[$FeCl_4$]/CNT-1∼3 and Bmim[$FeCl_4$]/CNT were obtained after removing the methanol through a rotary evaporator and vacuum drying at 50 °C. The details of the material can be found in Table 1.

2.3. Characterization of morphologies and chemical structure

The morphologies of each sample were analyzed by a field-emission scanning (SEM) and transmission (TEM) electron microscope (SEM, Zeiss Gemini 300, Carl Zeiss Jena Ltd., Germany, TEM, JEM-2100, JEOL Ltd., Japan). Raman spectra (inVia, Renishaw Ltd., Britain) were recorded on a spectrometer with a 633 nm laser. Fourier transform infrared spectroscopy (FT-IR) was performed via a PerkinElmer Spectrum Two FT-IR Spectrometer using the KBr pellet technique. X-ray photoelectron spectroscopy (XPS) measurement of MIL/CNT was carried out via a KRATOS AXIS-ULTRA DLD spectrometer using Al-Kα radiation.

Table 1
Sample names, the amounts of CNT, $FeCl_3$, and imidazolium salt added for the preparation of MIL/CNT.

Sample name	CNT (mg)	$PIMSO_3$ (g)	[Bmim]Cl (g)	$FeCl_3$(g)
Bmim[$FeCl_4$]/CNT	500	0	1.746	1.62
$PIMSO_3$Bim[$FeCl_4$]/CNT-1	300	0.68	0.873	1.62
$PIMSO_3$Bim[$FeCl_4$]/CNT-2	500	0.68	0.873	1.62
$PIMSO_3$Bim[$FeCl_4$]/CNT-3	800	0.68	0.873	1.62

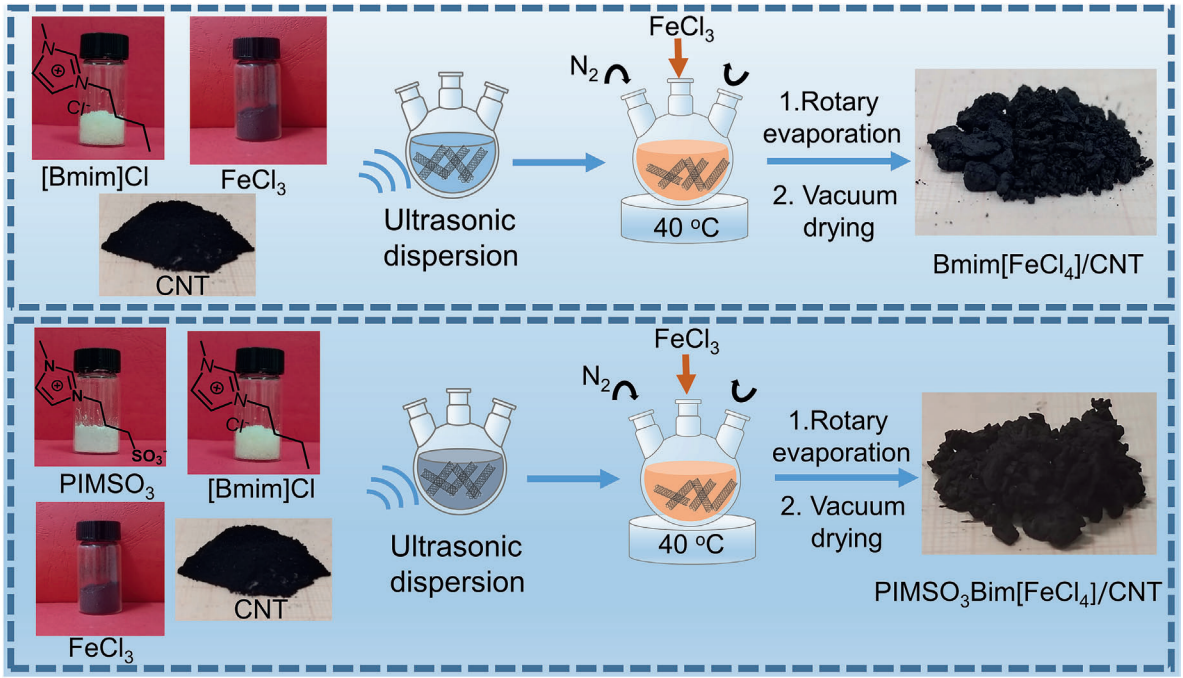

Fig. 1. Fabrication progress of MIL/CNTs.

2.4. Measurement of electromagnetic and EMW absorption performance

EMW absorption tested samples were prepared by uniformly mixing samples and paraffin with a mass ratio of 1:5. Then, the mixtures were pressed into cylinder-shaped EMW absorbers (Φ_{out} = 7.00 mm, Φ_{in} = 3.00 mm). Employed the vector network analyzer (VAN, Agilent N5245A) to get the electromagnetic parameters of the EMW absorber, the permittivity and permeability of real parts (ε′, μ′) and imaginary parts (ε″, μ″), in the frequency range of 2–18 GHz through the built-in algorithm of VAN based on transmission line theory. The EMW absorption performances, which were evaluated by Reflect Loss (RL), are obtained through calculated electromagnetic parameters of samples using equations (1) and (2) [25–27]. Where Z_0 is the impedance of air, Z_{in} is the normalized input impedance of the materials, c is the light velocity, f is the electromagnetic wave frequency, d is the thickness of the material, and ε_r and μ_r represent the complex permittivity and permeability of the composite medium, respectively.

$$\mathrm{RL(dB)} = 20\,lg\left|\frac{Z_{in}\text{-}Z_0}{Z_{in}+Z_0}\right| \tag{1}$$

$$Z_{in} = Z_0\sqrt{\frac{\mu_r}{\varepsilon_r}}tanh\left[\mathrm{j}\left(\frac{2\pi fd}{c}\right)\sqrt{\mu_r\varepsilon_r}\right] \tag{2}$$

The Four Prode apparatus (ST-2258, Suzhou Jingge Electronics Co Ltd., China) was used to measure the electrical conductivities of MIL, CNT and MIL/CNT. Magnetic measurements were conducted with a superconducting quantum interference device (SQUID, MPMS XL-7, Quantum Design). The arch method testing system with VAN (3671G, Ceyear Co Ltd., China) was employed to measure the RL values of the sample directly. The testing sample was prepared for the panel with a

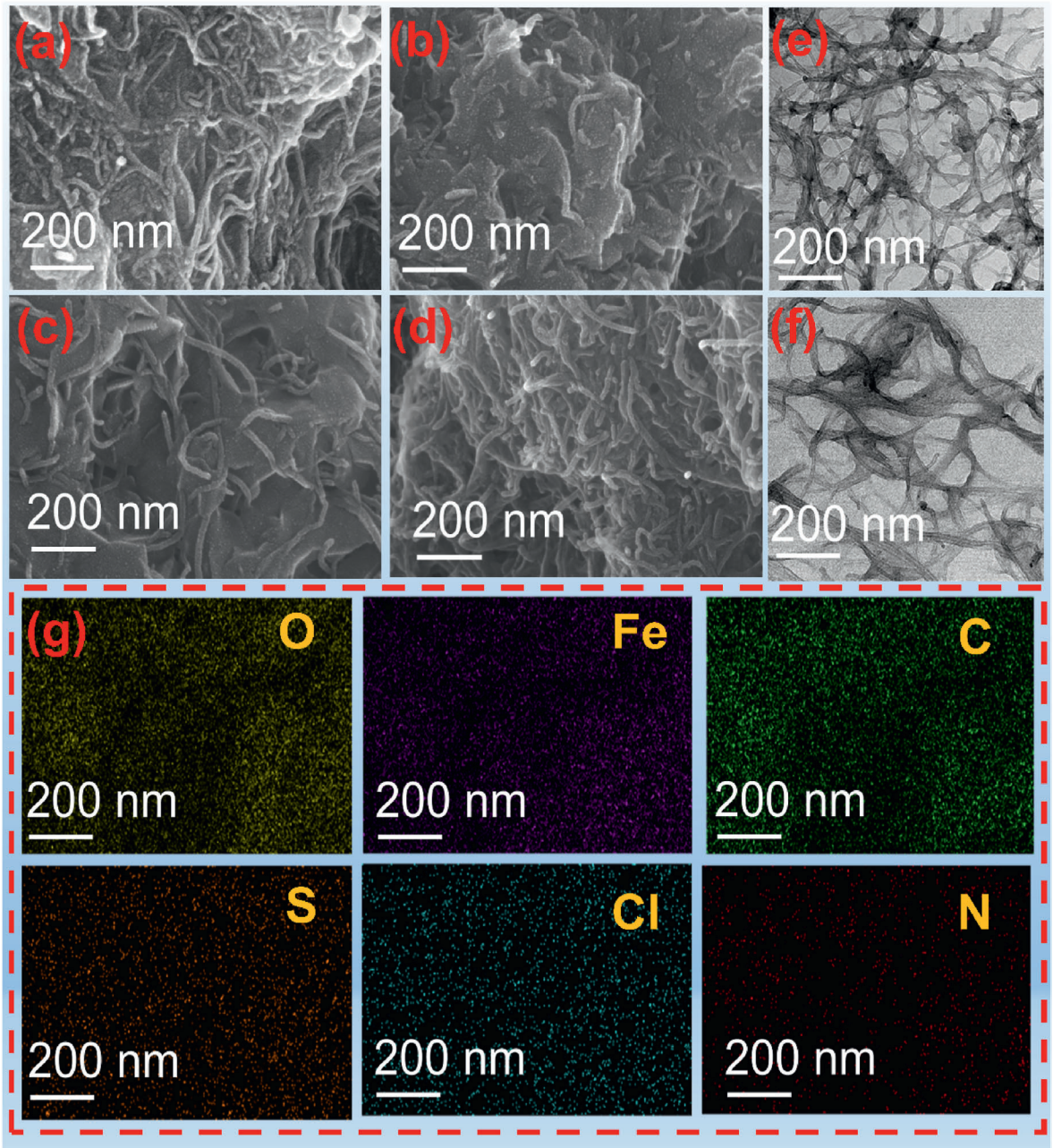

Fig. 2. SEM images of (a) Bmim[$FeCl_4$]/CNT and (b–d) PIMSO_3Bim[$FeCl_4$]/CNT-1∼3, TEM images of (e) PIMSO_3Bim[$FeCl_4$]/CNT-2 and (f) Bmim[$FeCl_4$]/CNT, (g) EDS mapping of PIMSO_3Bim[$FeCl_4$]/CNT-2.

size of 180*180 mm before the test. The dielectric properties of MILs were measured using an open-ended coaxial probe system linked with the vector network analyzer (VAN, Agilent N5245A)

3. Results and discussion

3.1. Structure, morphology and properties of MIL/CNT and MIL

Macroscopic Bmim[$FeCl_4$]/CNT and $PIMSO_3$Bim[$FeCl_4$]/CNT are gel-like solids, as shown in Fig. 1. The gel-like states of MIL/CNT mainly depend on the MIL. Similar to the prepared procedures of MIL/CNT, the corresponding MILs were synthesized without CNT. The Bmim[$FeCl_4$] and $PIMSO_3$Bim[$FeCl_4$] are both black liquids at room temperature (Fig. S1a). Among the two MILs, the $PIMSO_3$Bim[$FeCl_4$] exhibits higher viscosity, approximately 15 Pa S, than Bmim[$FeCl_4$] (0.005 Pa S) in Fig. S1b. The $PIMSO_3$Bim[$FeCl_4$] with higher viscosity can be tightly combined with CNT.

The microstructures of Bmim[$FeCl_4$]/CNT and $PIMSO_3$Bim[$FeCl_4$]/CNT were investigated by SEM and TEM images as shown in Fig. 2. In Fig. 2a–d, the SEM images of each MIL/CNT express that the CNT, as the skeleton, builds the three-dimensional (3D) network to tightly combine with the Bmim[$FeCl_4$] and $PIMSO_3$Bim[$FeCl_4$], respectively. Meanwhile, Fig. 2b displays the CNT covered by $PIMSO_3$Bim[$FeCl_4$] and the CNT can be seen increasingly exposed with increasing the CNT content in Fig. 2c and d. The TEM images of $PIMSO_3$Bim[$FeCl_4$]/CNT (Fig. 2e) and Bmim[$FeCl_4$]/CNT (Fig. 2f) present the MIL loaded on the 3D network of CNT. The SEM and TEM images demonstrate that the liquid MILs (Bmim[$FeCl_4$] and $PIMSO_3$Bim[$FeCl_4$]) are tightly and stably bound to the solid CNTs to form the composite. This strong association results from cation-π and π-π interactions involving the imidazolium cations [19,20]. Furthermore, the EDS mappings (Fig. 2g) expose the C, N, O, S, Fe, and Cl elements in the $PIMSO_3$Bim[$FeCl_4$]/CNT.

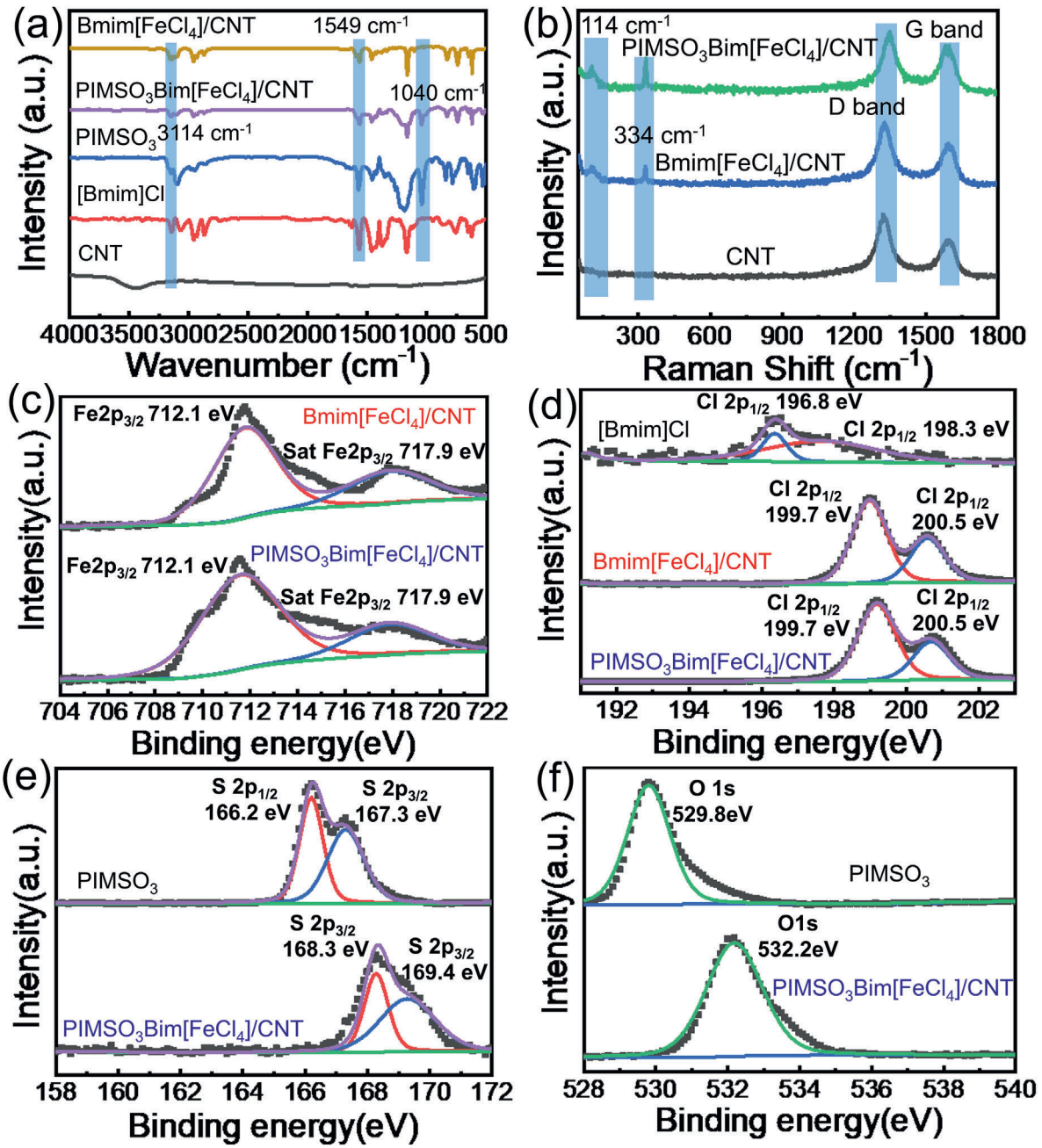

Fig. 3. (a) FT-IR, (b) Raman and XPS spectra of MIL/CNT: (c) Fe 2p, (d) Cl 2p, (e) S 2p and (f) O 1s spectra.

The Spectral analysis results (Fig. 3 and Fig. S2) further express the detailed chemical structure of MIL/CNT and MIL. In the FT-IR spectra of MIL/CNTs (Fig. 3a), the absorption peaks at 1549 cm^{-1} and 3114 cm^{-1} are attributed to C=N and C-H in the imidazole ring [28–30], which appear in the FT-IR spectrum of $PIMSO_3$ and [Bmim]Cl. Contrary to the FT-IR spectra of CNT without obvious absorption peaks, the apparent absorption peak of C=N (1549 cm^{-1}) similarly appears on the FT-IR spectrum of MIL/CNT, also reflecting the existence of the imidazole ring in MIL/CNT. The FT-IR spectrum of $PIMSO_3Bim[FeCl_4]$/CNT shows a signature peak of SO_3^- at 1040 cm^{-1} [29–32], which is absent in the $Bmim[FeCl_4]$/CNT spectrum, verifying the distinct chemical structures. Moreover, the FT-IR spectra of MIL/CNT are similar to the corresponding MIL (Fig. S2a). Fig. 3b displays the Raman spectra of MIL/CNT and CNT, respectively. The D band at 1347 cm^{-1} and the G band at 1581 cm^{-1} are assigned to typical Raman peaks of CNT, which exhibit the lattice defects of carbon atoms and tensile vibration of in-plane sp2 hybridization, respectively. The intensity ratio of the D and G bands (I_D/I_G) of pure CNT is 1.20. After the CNT is composited with MIL, the I_D/I_G values of MIL/CNT decrease to 1.14–1.17. Although the I_D/I_G values of MIL/CNT are lower than CNT, their I_D/I_G values still approach CNT, indicating that the lattice and Sp2 hybridization of CNT do not destroy. Moreover, the Raman peaks at 334 cm^{-1} and 114 cm^{-1} can be found in the Raman spectra of three MIL/CNTs, respectively. Remarkably, these absorption peaks (334 and 114 cm^{-1}) simultaneously appear in the Raman spectrum of MIL (Fig. S2b). These Raman peaks were assigned to the symmetric stretching and bending of Fe^{3+} complexing anions ($[FeCl_4]^-$ and $[FeSO_3Cl_3]^-$) [33,34]. Meanwhile, to explore the structure of Fe^{3+} complexing anions, XPS was employed to investigate the chemical composition of three magnetic burkey gels as shown in Fig. S3 and Fig. 3c–f. In Fig. S3, signals of C, O, Fe, Cl, S and N elements are observed in the XPS survey spectra. The Fe 2p spectra (Fig. 3c) present two peaks at 712.1 and 717.9 eV, which are attributed to Fe 2p3/2 and Fe satellite peak, respectively [35,36]. In Fig. 3d, the Cl 2p peaks at 196.8 and 198.3 eV could be related to imidazolic chloride salt and organic chloride [35]. After complexing with $FeCl_3$, the Cl 2p peaks of $Bmim[FeCl_4]$/CNT and $PIMSO_3Bim[FeCl_4]$/CNT significantly shift to high binding energy. Among all the MIL/CNT, the Cl 2p peaks at 199.7 and 200.5 eV are attributed to metal chlorine (Fe-Cl) and organic chloride [37]. In Fig. 3e, the S2p peaks at 166.2 and 167.3 eV are assigned to the S2p1/2 and S2p3/2 from SO_3^- of $PIMSO_3$ [38,39]. After complexing with $FeCl_3$, the S2p peaks of $PIMSO_3Bim[FeCl_3]$/CNT move to high binding energy (168.3 and 169.4 eV). Similarly, the O1s peak of SO_3^- also shifts to high binding energy when $PIMSO_3$ is complexed with Fe^{3+}(Fig. 3f). The movement of S2p and O1s peaks can prove the coordination effect between Fe^{3+} and $PIMSO_3$, which form the complexing ions ($[FeSO_3Cl_3]^-$).

Based on the Raman and XPS spectra, the formation of MIL is illustrated in Fig. S1c. For the $Bmim[FeCl_4]$, the Fe^{3+} coordinates with the Cl^- in [Bmim]Cl to form the complexing anions ($[FeCl_4]^-$). Subsequently, the $[FeCl_4]^-$ combined with the imidazolium cation (IM^+) to form the $Bmim[FeCl_4]$. In the $Bmim[FeCl_4]$, because the ion pairs of IM^+-$[FeCl_4]^-$ lack interaction, the $Bmim[FeCl_4]$ expresses the liquid state with low viscosity at room temperature. Similarly, in $PIMSO_3Bim[FeCl_3]$, the SO_3^- in the $PIMSO_3$ coordinate with Fe^{3+} to form the complexing anions ($[FeSO_3Cl_3]^-$), and because of the special zwitterionic structure, each IM^+-$[FeSO_3Cl_3]^-$ ion pairs are linked by the covalent bonds. Moreover, the zwitterionic structure results in the stronger ion-dipole or dipole-dipole interaction between the IM^+-$[FeSO_3Cl_3]^-$ and IM^+-$[FeCl_4]^-$ [28,29]. Therefore, the $PIMSO_3Bim[FeCl_4]$ is an ionic liquid with high viscosity.

The magnetic properties of the MIL and MIL/CNT are presented in Fig. 4. The macroscopic magnetic phenomena of liquid $Bmim[FeCl_4]$

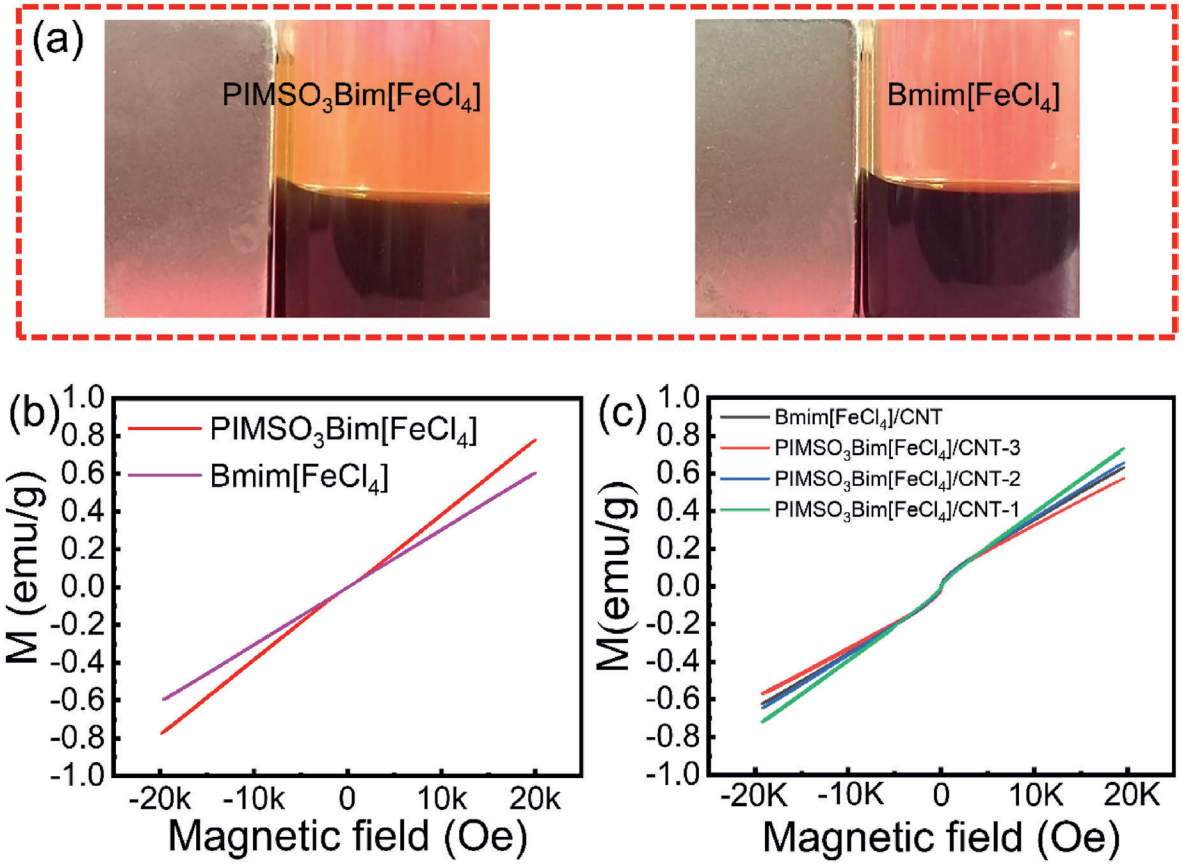

Fig. 4. (a) macroscopic magnetic phenomena of $Bmim[FeCI_4]$ and $PIMSO_3Bim[FeCI_4]$, (b) Magnetization curves of $PIMSO_3Bim[FeCI_4]$ and $Bmim[FeCl_4]$ and (c) magnetization curves of MIL/CNT.

and $PIMSO_3Bim[FeCl_4]$, attracted by a magnet, are exhibited in Fig. 4a. The magnetization curves of MIL (Fig. 4b) express the paramagnetic properties of two MILs. Their magnetic performance is attributed to the $[FeCl_4]^-$ and $[FeSO_3Cl_3]^-$ [16,24]. The saturation magnetizations (Ms) of $PIMSO_3Bim[FeCl_4]$ and $Bmim[FeCl_4]$ are 0.8 and 0.6 emu/g, respectively. The slightly higher Ms in $PIMSO_3Bim[FeCl_4]$ is mainly attributed to the restrained thermal motion of $[FeCl_4]^-$ and $[FeSO_3Cl_3]^-$ by the zwitterion [33]. After being composited with CNT, the magnetization curves of MIL/CNT still reflect paramagnetic (Fig. 4c). The Ms of $Bmim[FeCl_4]$/CNT and $PIMSO_3Bim[FeCl_4]$/CNT-1∼3 are 0.60, 0.74, 0.65, and 0.57 emu/g. Increasing the content of MIL boosts the Ms of MIL/CNT.

The conductivities of MIL, CNT and MIL/CNT were summarized in Table 2. Attributed to the ionic conduction caused by migration of IM^+ and $[FeCl_4]^-$, the $Bmim[FeCl_4]$ expresses the conductivity of $0.820*10^{-2}$ S/cm. Inducing the zwitterion, the ionic migration has been weakened in $PIMSO_3Bim[FeCl_4]$ due to the strong interaction of ion-dipole. Thus, the conductivities of $PIMSO_3Bim[FeCl_4]$ decline to $0.046*10^{-2}$ S/cm. The conductivities of MIL/CNTs are higher than those of MIL due to the CNT with high conductivity (>105 S/cm). The conductivities of $Bmim[FeCl_4]$/CNT and $PIMSO_3Bim[FeCl_4]$/CNT-1∼3 are 7.1, 3.93, 6.36 and 18.51 S/cm, which constantly rising with increasing the CNT content.

3.2. Electromagnetic wave absorbing performance and mechanism

The EMW absorption performance of CNT, $Bmim[FeCl_4]$/CNT and $PIMSO_3Bim[FeCl_4]$/CNT-1∼3 was evaluated by the Reflect Loss (RL). The RL of each based EMW absorber is calculated by equations (1) and (2). Generally, the values of RL require less than −10 dB to achieve the optimal EMW absorbing performance. The EWAM with Optimal performance requires both strong absorbing strength and a broad bandwidth. Figure S4 and Fig. 5 present RL curves and 2D RL contour plots of different EWAM, respectively, illustrating the RL values and effective absorption bands (EABs). The CNT based EMW absorber with poor EMW absorption performance (RL > −10 dB) is presented in Fig. S4a. On the contrary, the RL curves of all MIL/CNT based EMW absorbers fall below −10 dB with different thicknesses as shown in Fig. S4b–e, indicating the effective EMW absorbing performance of MIL/CNT. In the 2D RL contour plots (Fig. 5), the regions enclosed by dashed lines are the regions of RL < −10 dB, presenting the EABs of the MIL/CNT based EMW absorbers.

In Fig.S4b and Fig. 5a, the $Bmim[FeCl_4]$/CNT based EMW absorber could reach −32 dB of minimum reflection loss (RL_{min}) with 2.8 mm thickness at 11.0 GHz and 5.2 GHz (7.04–12.24 GHz) of EAB_{max} with 3.1 mm. For the $PIMSO_3Bim[FeCl_4]$/CNT-1 based EMW absorber, as shown in Fig. S4c and Fig. 5b, RL_{min} reaches −44 dB with 2.1 mm at 14.5 GHz, and the EAB_{max} extends to 6.7 GHz (7.6–14.3 GHz) at 2.7 mm of thickness. As the content of CNT increases, the EAB_{max} and RL_{min} of $PIMSO_3Bim[FeCl_4]$/CNT-2 based EMW absorber further enhance as exhibited in Fig. S4d and Fig. 5c. RL_{min} achieves −46 dB with 2.1 mm at 15.8 GHz. Notably, its EAB_{max} extends to 7.5 GHz (9.44–16.94 GHz) at a lower matching thickness (2.4 mm). However, excessive content of CNT leads to poor EMW absorbing performance of $PIMSO_3Bim[FeCl_4]$/CNT-3 based EMW absorber, presented in Fig.S4e and Fig. 5d. Although the EAB_{max} and RL_{min} of $PIMSO_3Bim[FeCl_4]$/CNT-3 based EMW absorber are all achieved in the thickest thickness (1.8 and 1.6 mm), the EAB_{max} and RL_{min} are only 5.4 GHz (10.64–16.04 GHz) and −30 dB, respectively. The above EMW absorbing performances reflect that the excellent EMW absorbing performance with super broadband absorption can be achieved in the $PIMSO_3Bim[FeCl_4]$/CNT-1∼2 containing the zwitterion structure and a suitable content of CNT.

Table 2
The conductivities of CNT and MIL/CNT

Sample	Conductivity (S/cm)
CNT	>105[a]
$Bmim[FeCl_4]$	0.82^a10^{-2}
$PIMSO_3Bim[FeCl_4]$	0.046^a10^{-2}
$Bmim[FeCl_4]$/CNT	7.1
$PIMSO_3Bim[FeCl_4]$/CNT-1	3.93
$PIMSO_3Bim[FeCl_4]$/CNT-2	6.36
$PIMSO_3Bim[FeCl_4]$/CNT-3	18.51

[a] The conductivity of CNT are beyond the measuring range of Four probe apparatus (105 S/cm).

Meanwhile, compared to other reported CNT based EMW absorbing materials as shown in Table 3, the MIL/CNT all present better EMW absorbing performance. Especially for $PIMSO_3Bim[FeCl_4]$/CNT-2 based EMW absorber, its EAB_{max} (7.5 GHz) exceeds others to a large degree. Additionally, the $PIMSO_3Bim[FeCl_4]$/CNT is selected to be mixed with Liquid Silicone Rubber and then cured to a composite with a size of 180*180*2.3 mm as shown in Fig. S5a. After the directly test by arch method, the EMW absorbing performance of the composite is exhibited in Fig. S5b, which achieve the RL_{min} of −26 dB and EAB of 6.88 GHz.

The EMW absorbing capacity of EWAM is tightly dependent on their electromagnetic parameters, relatively complex permittivity ($\varepsilon_r=\varepsilon'-j\varepsilon''$) and permeability ($\mu_r=\mu'-j\mu''$). The permittivity and permeability of real parts (ε', μ') and imaginary parts (ε'', μ'') represent the storage and dissipation of electromagnetic energy, respectively [49,50]. As shown in Fig. 6a and b, the ε' and ε'' of MIL/CNT based EMW absorbers are located in ranges of 4–18 and 2–8, respectively, which is far less than the CNT due to the lower conductivities of MIL/CNT (Table 2). The subfigures in Fig. 6a and b present the difference of ε' and ε'' curves between all MIL/CNT based EMW absorbers. The ε' of the $Bmim[FeCl_4]$/CNT and $PIMSO_3Bim[FeCl_4]$/CNT-1∼2 are approximate as shown in the subfigure of Fig. 6a, locating on 12–6.5. However, the ε' of $PIMSO_3Bim[FeCl_4]$/CNT-3 based EMW absorber increase to 16∼8 with the rise of CNT content. In the subfigure of Fig. 6b, the ε'' values of $PIMSO_3Bim[FeCl_4]$/CNT-1∼3 are surpass $Bmim[FeCl_4]$/CNT based EMW absorber and achieve the highest ε'' values in $PIMSO_3Bim[FeCl_4]$/CNT-3 EMW absorber at most ranges of 2–18 GHz. According to the free electron theory, higher ε'' values are mainly determined by strong conductivity (σ), the towering ε'' values of CNT based EMW absorber result in the highest conductivity of CNT (Table 2). The conductivities of MIL/CNTs are far below CNT due to MIL hindering the electronic migration, which leads to the decline of ε''. Similarly, the ε'' values of $PIMSO_3Bim[FeCl_4]$/CNT-3 based EMW absorber surpass other MIL/CNT based EMW absorbers due to the higher conductivity of $PIMSO_3Bim[FeCl_4]$/CNT-3. However, the $PIMSO_3Bim[FeCl_4]$/CNT-2 shows approximate conductivity to $Bmim[FeCl_4]$/CNT, even the conductivity of $PIMSO_3Bim[FeCl_4]$/CNT-1 are obvious lower than $Bmim[FeCl_4]$/CNT, the ε'' values of $PIMSO_3Bim[FeCl_4]$/CNT-1∼2 based EMW absorber are still higher than $Bmim[FeCl_4]$/CNT. Therefore, other factors also contribute to ε'' values. Generally, the ε'' of MIL/CNT are composed of conduction (ε_c'') and polarization (ε_p'') loss as present in equations. (3) and (4) [26,51,52]. Meanwhile, many resonance peaks, reflecting polarization relaxation process, can be observed in ε'' curves of MIL/CNT [53,54]. Notably, the resonance peaks of $PIMSO_3Bim[FeCl_4]$/CNT-1∼3 EMW absorber show stronger amplitude than $Bmim[FeCl_4]$/CNT, revealing the existence of a stronger polarization relaxation process in the $PIMSO_3Bim[FeCl_4]$/CNT.

$$\varepsilon'' = \varepsilon_p'' + \varepsilon_c'' \tag{3}$$

$$\varepsilon_c'' = \frac{\sigma}{2\pi f \varepsilon_0} \tag{4}$$

As shown in Fig. 6c and d, the μ' and μ'' values of the CNT-based EMW absorber stably approach 1 and 0, respectively, confirming its non-magnetic response. In contrast, the μ' and μ'' curves of the MIL/CNT composites fluctuate across the 2–18 GHz band, indicating a uniformly weak magnetic response to the electromagnetic field.

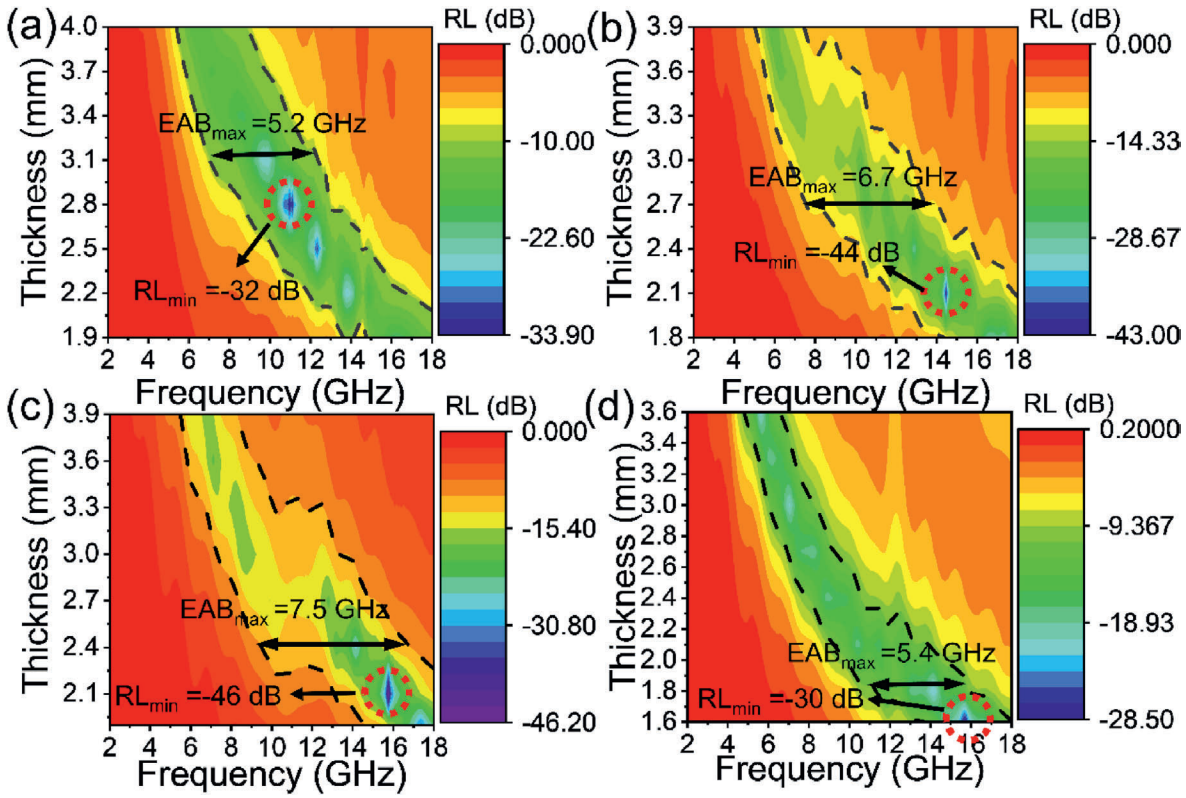

Fig. 5. 2D RL contour plots of each MIL/CNT based EMW absorber: (a) Bmim[$FeCl_4$]/CNT, (b) $PIMSO_3$Bim[$FeCl_4$]/CNT-1, (c) $PIMSO_3$Bim[$FeCl_4$]/CNT-2 and (d) $PIMSO_3$Bim[$FeCl_4$]/CNT-3.

Table 3
Summarized EMW absorption performance of CNT based EMW absorbing materials reported in previous papers.

Samples	RL_{min} (dB)	EAB_{max} (GHz) (RL < −10 dB)	Thickness (mm)	Ref
FeCo/CNTs/HNTs	−57.77	6.24	3.0	[11]
liquid-like Fe_3O_4/CNT	−52.57	5.2	1.4	[15]
P[AVIm][$FeCl_4$]/CNT/rGO	−51.03	5.63	2.2	[34]
SiC@Co-CNT	−57.67	2.63	3.75	[40]
CoO/CNT	−25.9	4.5	3	[41]
FeCo/Cu/CNT	−48.1	5.76	1.8	[42]
CNT/$BaFe_{12}O_{19}$	−43.9	3.9	4.5	[43]
CNT-rGO-Co/Ni-MOF	−43	4	1.5	[44]
r-GO/a-CNT/NCS	−35.8	2.7	2.3	[45]
CoNiZnFe_2O_4@CNT	−30.11	4.11	3.0	[46]
Ti_3C_2Tx@CNTs/Ni	−64.60	6.1	2.7	[47]
MOF-derived Ni@CNT	−44.40	4.3	1.5	[48]
$PIMSO_3$Bim[$FeCl_4$]/CNT-2	−46	7.5	2.4	This work

For the Bmim[$FeCl_4$]/CNT and $PIMSO_3$Bim[$FeCl_4$]/CNT-1∼3 based EMW absorbers, the μ' values range from 1.17–0.93, 1.58–0.97, 1.41–0.89, and 1.32–1.02, respectively, showing a positive correlation with the Ms of the corresponding MIL/CNT composites. Correspondingly, their μ'' values fall within the ranges of 0.24–0.013, 0.35–0.03, 0.36–0.07, and 0.23∼(−0.07), respectively. Notably, multiple resonance peaks are observed, suggesting the presence of multiple magnetic resonance behaviors [50,51,54].

Based on the above electromagnetic parameters, the EMW dissipating capacity and routes are exhibited in Fig. 7. The electric and magnetic dissipating capacities are gradually depicted by loss tangent ($tan\ \delta_E = \varepsilon''/\varepsilon'$ and $tan\ \delta_M = \mu''/\mu'$) [47,55]. In Fig. 7a, the $tan\ \delta_E$ of pure CNT EMW absorber tower over other MIL/CNT based EMW absorbers, indicating its strong dielectric loss ability. Meanwhile, the $PIMSO_3$Bim[$FeCl_4$]/CNT-1∼2 based EMW absorbers exhibit higher $\tan\delta_E$ values than $PIMSO_3$Bim[$FeCl_4$]/CNT-3 and Bmim[$FeCl_4$]/CNT at most frequency ranges, as shown in Fig. 7b, proving the strong dielectric loss capacity of the $PIMSO_3$Bim[$FeCl_4$]/CNT-1∼2. The dielectric loss mainly contributed to conductance and polarization loss. According to the Debye relaxation theory, the ε'–ε'' curves of all EMW absorbers are plotted through equations (S1-S3) as shown in Fig. S6 and Fig. 7c. The ε'–ε'' curves consist of semicircles or lines, which represent the conductance and polarization loss, respectively [5,44]. The ε'–ε'' curve of the CNT based EMW absorber approach a long tail (Fig. S6), reflecting that the conductance loss is the primary contributor to dielectric loss. The ε'-ε'' curves of MIL/CNT based EMW absorber are composed of straight lines and many semicircles (Fig. 7c), confirming the co-existence of conduction and multiple polarization loss. The conduction loss results from the electron conduction of CNT and ionic conduction of IM^+-[$FeCl_4$]$^-$ in MIL. Linear segments gradually emerge and exhibit a trend of increasing slope in the ε'-ε'' curves of $PIMSO_3$Bim[$FeCl_4$]/CNT based EMW absorbers, indicating an enhancement of conduction loss with increasing conductivity. The multiple polarization loss includes the interfacial and dipole polarization losses. Remarkably, the $PIMSO_3$Bim[$FeCl_4$]/CNT-1∼3 based EMW absorbers present semicircles with the bigger diameter compared to Bmim[$FeCl_4$]/CNT, which revealed richer polarization loss [1]. The stronger polarization loss may result from the zwitterion-enhanced dipole polarization. To further verify the perspective, the permittivities of Bmim[$FeCl_4$] and $PIMSO_3$Bim[$FeCl_4$] have been directly tested (Fig. S7a and b). Compared to the ε'-ε'' curves of two MILs in Fig. S7c and d. The semicircles in the ε'-ε'' curves of $PIMSO_3$Bim[$FeCl_4$] also exhibit the bigger diameter than Bmim[$FeCl_4$], reflecting more polarization behavior in $PIMSO_3$Bim[$FeCl_4$]. Meanwhile, we calculated the ε_p'' and ε_c'' by equations (3) and (4) as shown in Fig. S7e and f, respectively. The ε_c'' of Bmim[$FeCl_4$] are higher than ε_p'' at 2–13.2 GHz

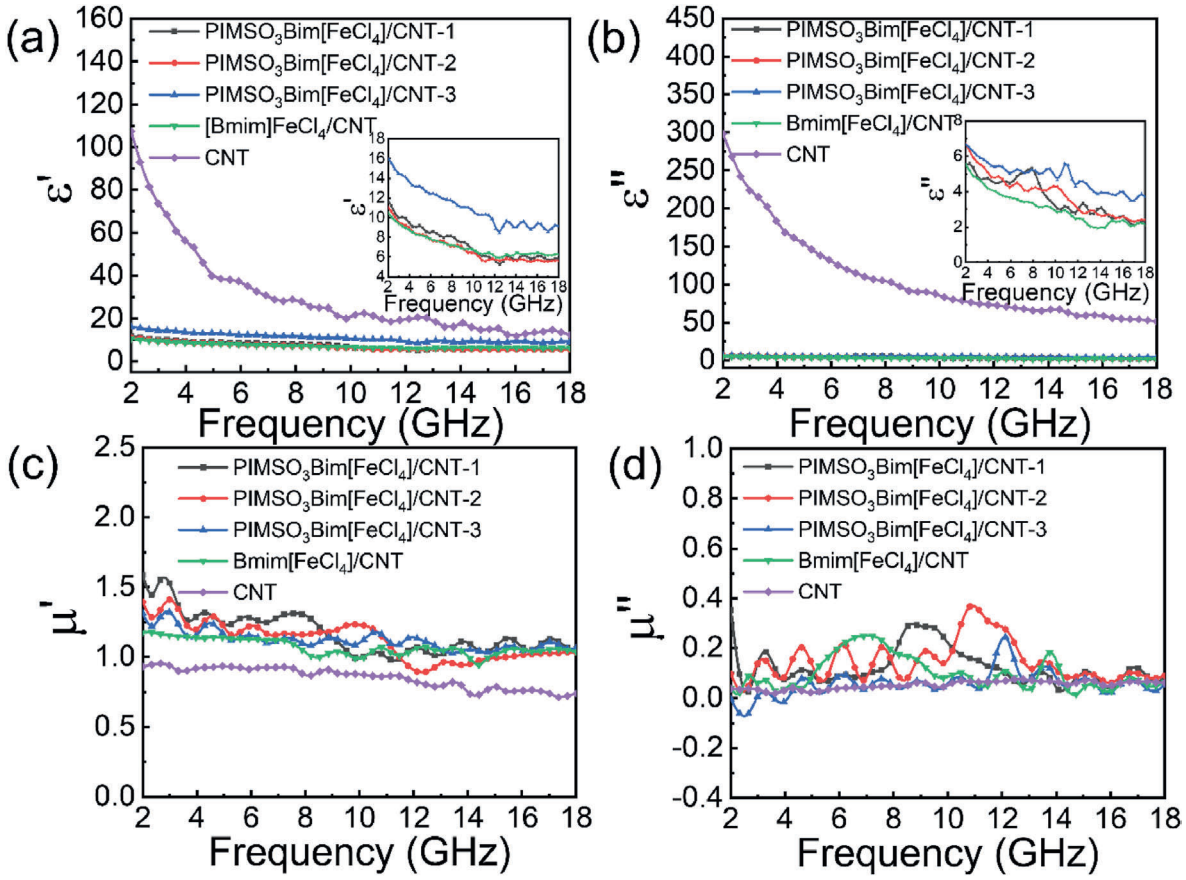

Fig. 6. Permittivity and permeability of EMW absorber: (a) real (ε′) and (b) imaginary parts (ε") of complex permittivity, (c) real (μ′) and (d) imaginary parts (μ") of complex permeability.

and lower at 13.2–18 GHz (Fig. S7e). However, the ε_p'' of $PIMSO_3Bim[FeCl_4]$ totally surpass ε_c'' at 2–18 GHz (Fig. S7f). Moreover, the average contribution ratios of ε_p'' in $Bmim[FeCl_4]$ and $PIMSO_3Bim[FeCl_4]$ are 44 % and 89 %, respectively. The data clearly demonstrate a more dominant role of polarization loss in $PIMSO_3Bim[FeCl_4]$. Furthermore, the electrostatic potential maps (EPS) of $Bmim[FeCl_4]$ and $PIMSO_3Bim[FeCl_4]$ have been simulated through the Material Studio software based on Density Functional Theory (DFT), which visualizes the charge density (Fig. 7d). The positive and negative charges are displayed by orange and blue, respectively. The color transforming from darker to lighter in EPS corresponds to a decrease in local charge density. The more remarkable color difference observed in the zwitterion of $PIMSO_3Bim[FeCl_4]$ indicates enormous differences in charge distribution. Thus, zwitterion induces a higher electrostatic potential difference (0.2530 eV) than IM^+-$[FeCl_4]^-$ of $Bmim[FeCl_4]$ (0.2051 eV) as summarized in Table S1. The higher electrostatic potential difference results in an enhancement of the dipole moment. The dipole moment of $PIMSO_3Bim[FeCl_4]$ (15.41) is higher than $Bmim[FeCl_4]$ (9.21), which was calculated through the process as presented in the supporting information 1. Thus, the zwitterionic structure with a high dipole moment leads to the stronger dipole polarization loss in $PIMSO_3Bim[FeCl_4]$/CNT.

In Fig. 7e, different from the near-zero $\tan\delta_M$ of the non-magnetic CNT based EMW absorber, the MIL/CNT based EMW absorbers exhibit a measurable $\tan\delta_M$ (0.33 to −0.052), confirming the presence of magnetic loss in these composites. Among all MIL/CNT, the $PIMSO_3Bim[FeCl_4]$/CNT-3 based EMW absorber shows the lowest $\tan\delta_M$, consistent with its decline in Ms. Although the $\tan\delta_M$ values are smaller than the corresponding $\tan\delta_E$ values, the dielectric loss is the main dominating EMW loss route in MIL/CNT, the magnetic loss is not to be neglected. The C_0 ($C_0=\mu''(\mu')^{-2}f^{-1}$) parameters reveal the specific origin of magnetic loss as shown in Fig. 7f. The C_0 values tend to a constant in the frequency ranges, considering eddy loss [42]. However, the C_0 values of all MIL/CNT-based EMW absorbers vary across the 2–18 GHz band, indicating that their magnetic loss originates primarily from magnetic resonance behaviors caused by natural and exchange resonances [45–48].

The favorable impedance matching and high attenuation constants (α) are equally crucial factors for EWAM with outstanding performance, which guarantee the minimum reflection and strong attenuation of EMW, respectively. Attenuation constants (α) are typically calculated using Equation (5), and the normalized characteristic impedance values ($|Z_{in}/Z_0|$) are close to 1, indicating excellent impedance matching performance [11,49,50]. The high conductivity of CNT (>105 S/cm) endowed the prohibitively high permittivity ($\varepsilon' = 110\text{-}20$, $\varepsilon'' = 300\text{-}50$) and $tan\ \delta_E$ (2.8–4.5) in the CNT based EMW absorber, resulting in the highest values of α (449–1702) as present in Fig. S8. However, the excessive permittivity also leads to the values of $|Z_{in}/Z_0|$ far from 1 (Fig. 8a), leading to substantial reflection of EMW at the surface caused by severe impedance mismatch. Conversely, the proper ionic conduction of the MIL results in a composite (MIL/CNT) with lower conductivities (Table 2), which leads to the moderate permittivity ($\varepsilon' = 16\text{–}6.5$ and $\varepsilon'' = 6.5\text{–}2$). Furthermore, the magnetic properties of MIL also contribute to the optimization of impedance matching. Thus, $|Z_{in}/Z_0|$ values of MIL/CNT based EMW absorber are closer to 1 than CNT (Fig. 8b–e), realizing the favorable impedance matching properties and minimum reflection of EMW.

In Fig. 8f, the α values of $PIMSO_3Bim[FeCl_4]$/CNT-1∼2 based EMW absorber approach to $Bmim[FeCl_4]$/CNT in 2–8 GHz, and then completely surpass $Bmim[FeCl_4]$/CNT in 8–18 GHz. It is reflected that the $PIMSO_3Bim[FeCl_4]$/CNT-1∼2 owns the stronger EMW attenuating

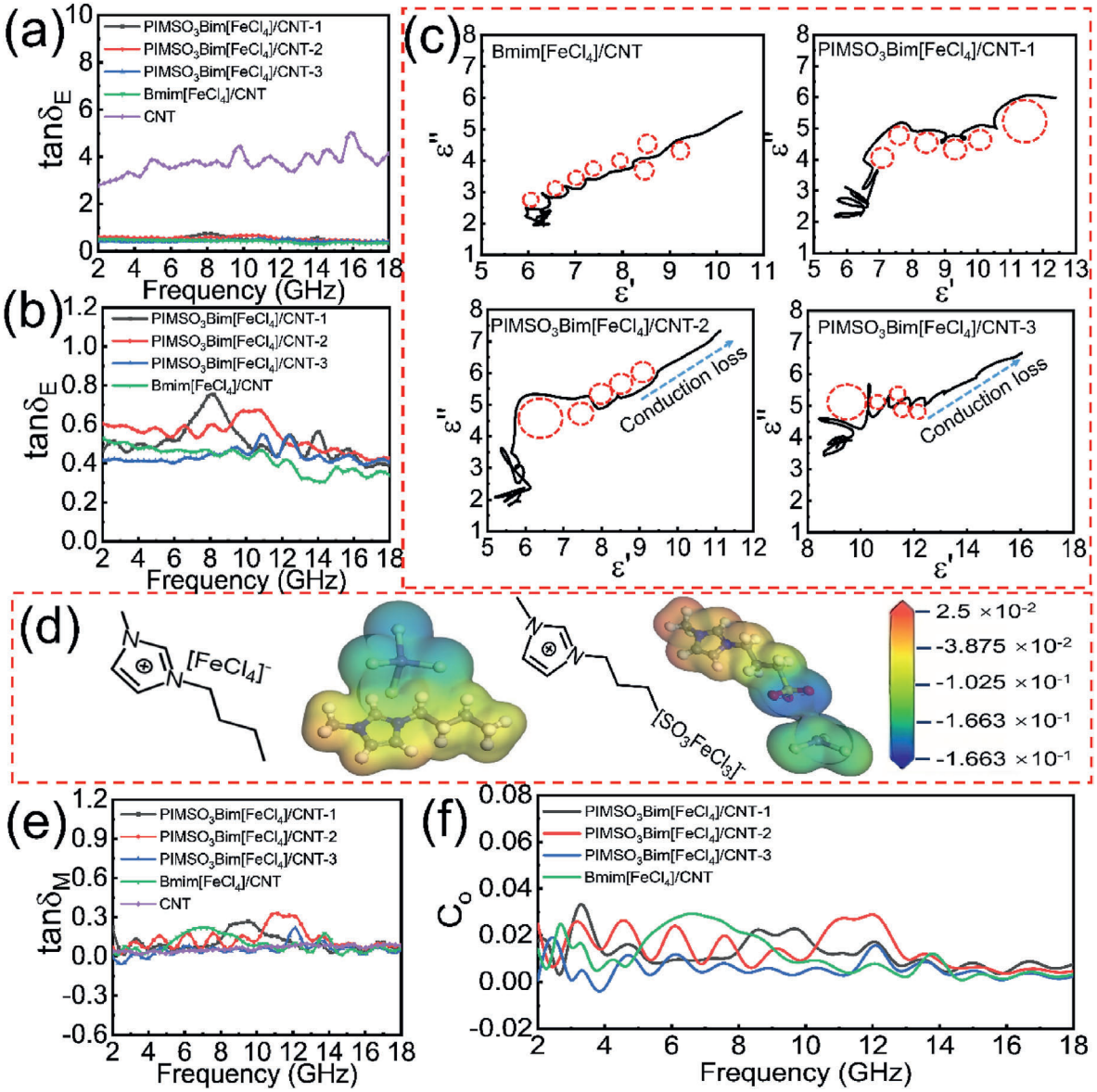

Fig. 7. (a, b) $\tan\delta_E$ curves of each EMW absorber, (c) ε'–ε'' curves of all MIL/CNT based EMW absorbers, (d) electrostatic potential maps of MIL, (e) $\tan\delta_M$ and (f) C_0 curves of MIL/CNT based EMW absorber.

capacity, driven by the zwitterion enhanced polarization loss. Thus, the $PIMSO_3Bim[FeCl_4]$/CNT-1~2 based EMW absorber presented better EMW absorbing performance than $Bmim[FeCl_4]$/CNT at 8–18 GHz. Although the α values of $PIMSO_3Bim[FeCl_4]$/CNT-3 based EMW absorber are also higher than $Bmim[FeCl_4]$/CNT at 8–18 GHz, even higher than $PIMSO_3Bim[FeCl_4]$/CNT-1~2 at 12–18 GHz, its EMW absorbing performance exhibits weakening. The main reason is that the higher conductivity in $PIMSO_3Bim[FeCl_4]$/CNT-3 triggered slight impedance mismatching.

$$\alpha = \frac{\sqrt{2}\pi f}{c}\sqrt{(\mu''\varepsilon''-\mu'\varepsilon') + \sqrt{(\mu''\varepsilon''-\mu'\varepsilon')^2 + (\mu'\varepsilon''+\mu''\varepsilon')^2}} \quad (5)$$

Synthesized the above discussions, the MIL, $PIMSO_3Bim[FeCl_4]$, combined with a certain amount of CNT to fabricate the $PIMSO_3Bim[FeCl_4]$/CNT. Appropriate impedance matching characteristics of the $PIMSO_3Bim[FeCl_4]$/CNT based EWM absorber enable EMW to effectively penetrate. Meanwhile, the strongest α values at a wide frequency range endow the $PIMSO_3Bim[FeCl_4]$/CNT-1~2 broadband EMW absorbing performance. The EMW is attenuated in the $PIMSO_3Bim[FeCl_4]$/CNT-1~2 through multiple dissipating routes as illustrated in Fig. 9. Firstly, the effective conductive network formed by CNT provides the paths for the jumping and migration of electrons, boosting the electron conductance loss (Fig. 9a) [46,54–56]. Secondly, besides the conductance loss of CNT, some freely moving ions(IM^+ and $[FeCl_4]^-$)in the $PIMSO_3Bim[FeCl_4]$ can migrate under the alternating electric field and trigger the ionic conductance loss to attenuate the EMW [57], as shown in Fig. 9b. Meanwhile, the zwitterions, which possess high dipole moments, formed multiple ion pairs and act as ionic dipoles [58]. The ionic dipoles serve as the polarization center, triggering stronger dipole polarization loss because their orientation cannot keep up with the alternating electric field [59–61]. Similarly, as shown in Fig. 9c, the heterojunction interfaces between the $PIMSO_3Bim[FeCl_4]$ and CNT lead to the attenuation of EMW through interfacial polarization loss [62,63]. Finally, the magnetic effect in $[FeCl_4]^-$ and $[FeSO_3Cl_3]^-$ certainly brings the magnetic loss for dissipating EMW [34,64] (Fig. 9d). The energy of EMW has been multiply attenuated through the synergistic coupling effect of magnetic and dielectric losses, which obtained the broadband EMW absorbing performance.

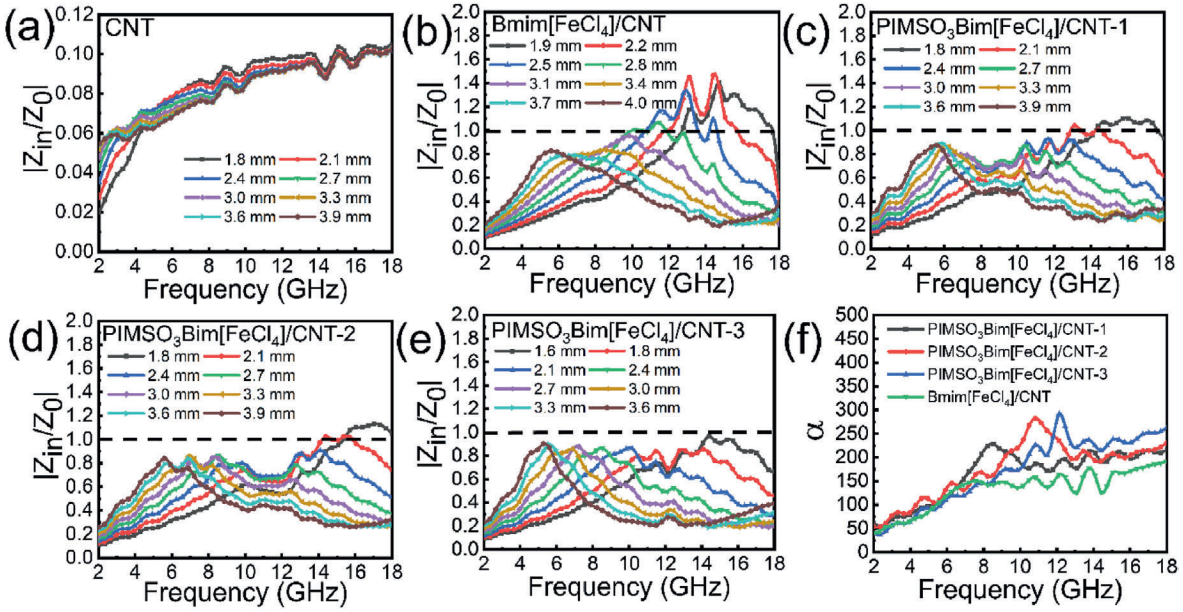

Fig. 8. Frequency dependence of $|Z_{in}/Z_0|$ curves of (a) CNT, (b) Bmim[$FeCl_4$]/CNT and (c–e) $PIMSO_3$Bim[$FeCl_4$]-1~3 based EMW absorber, (f) α curves of MIL/CNT based EMW absorber.

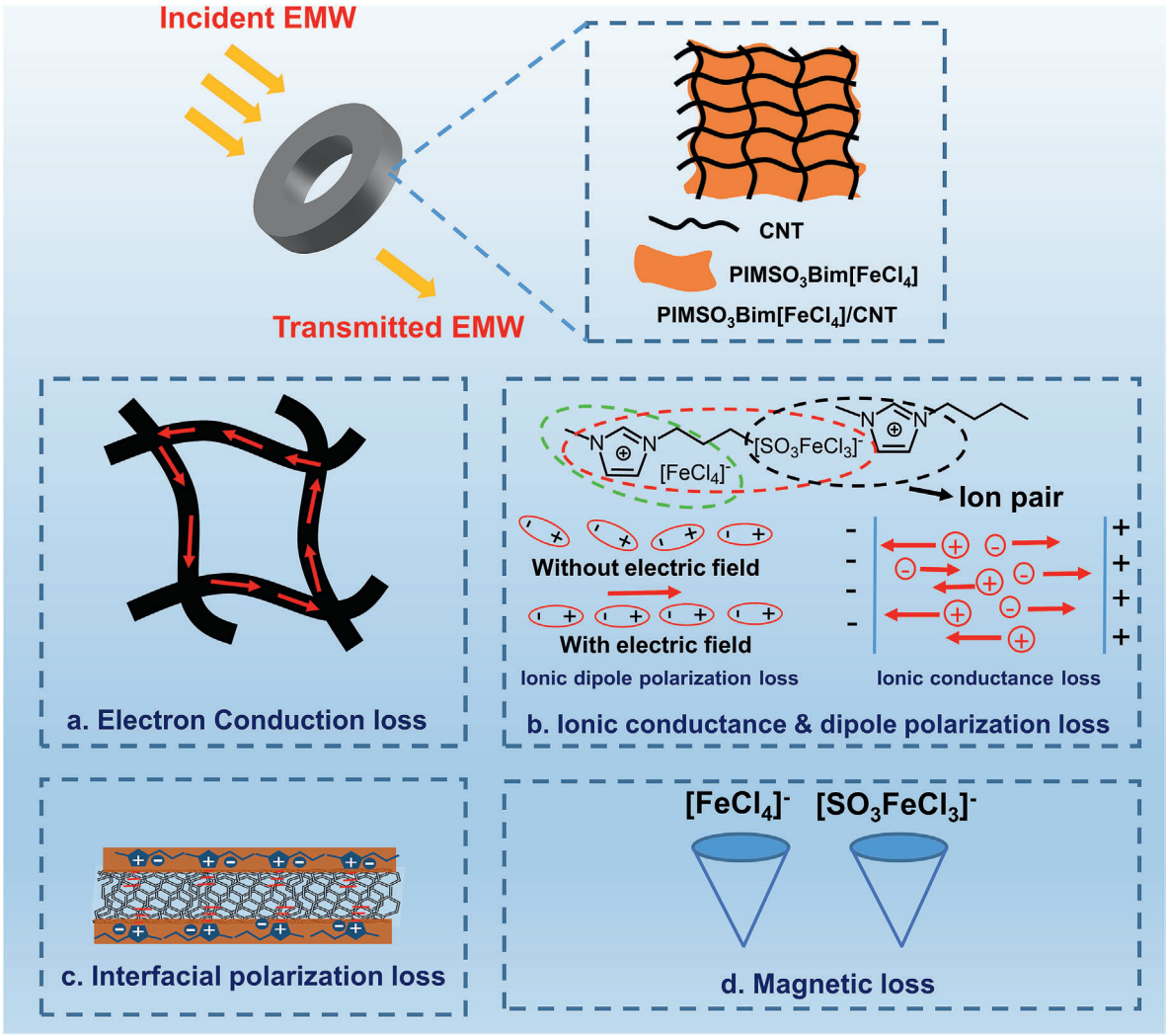

Fig. 9. Electromagnetic wave absorption mechanisms for Magnetic ionic liquid/CNT composite gel.

4. Conclusion

The two MIL/CNTs, $PIMSO_3Bim[FeCl_4]$/CNT and $Bmim[FeCl_4]$/CNT, were successfully fabricated in this paper. The MIL/CNTs expressed the satisfactory EMW absorbing performance due to favorable impedance matching properties and multiple EMW dissipating routes such as ionic conductance, polarization and magnetic loss. Notably, the $PIMSO_3Bim[FeCl_4]$/CNT with the zwitterionic structure presented better EMW absorbing performance than $Bmim[FeCl_4]$/CNT. The zwitterion deeply optimized the permittivities of $PIMSO_3Bim[FeCl_4]$/CNT, not only ensuring the suitable impedance matching performance, but also enhancing the polarization loss utilizing the high dipole moment. Therefore, the $PIMSO_3Bim[FeCl_4]$/CNT-2 based EMW absorber exhibited an RL_{min} of −46 dB and EAB_{max} of 7.5 GHz, achieving effective EMW absorption performance ($RL < -10$ dB) in the wide frequency range. The EAB_{max} of $PIMSO_3Bim[FeCl_4]$/CNT based EMW absorber shows wider than many reported CNT-based EMW absorption materials. The MIL/CNT composite demonstrates excellent broadband absorption, thus establishing it as a viable material for next-generation, multi-band electromagnetic defense and stealth applications.

CRediT authorship contribution statement

Chenjian Li: Writing – original draft, Methodology, Investigation, Data curation, Conceptualization. **Wenlai Xia:** Investigation, Data curation. **Dangfeng Zhou:** Visualization, Investigation. **Gang Lu:** Visualization, Investigation. **Hongmei Qin:** Data curation. **Shixian Zhang:** Writing – review & editing, Data curation. **Xueliang Jiang:** Project administration, Funding acquisition. **Chuanxi Xiong:** Project administration, Funding acquisition.

Funding

This work was financially supported by the National Natural Science Foundation of China (grant no. 51673154).

Declaration of competing interest

The authors declare that they have no known competing financial interests or personal relationships that could have appeared to influence the work reported in this paper.

Appendix A. Supplementary data

Supplementary data to this article can be found online at https://doi.org/10.1016/j.pnsc.2026.01.005.

References

[1] X. Su, J. Wang, X. Zhang, S. Huo, W. Chen, W. Dai, B. Zhang, Design of controlled-morphology $NiCo_2O_4$ with tunable and excellent microwave absorption performance, Ceram. Int. 46 (2020) 7833–7841, https://doi.org/10.1016/j.ceramint.2019.12.002.

[2] R. Wang, S. Ren, P. Chen, Multifunctional coaxial NC/Co/PPy nanotubes with efficient microwave absorption and thermal insulation properties, Chem. Eng. J. 524 (2025) 169721, https://doi.org/10.1016/j.cej.2025.169721. Chemical Engineering Journal.

[3] A. Ling, G. Tan, Q. Man, Y. Lou, S. Chen, X. Gu, R.W. Li, J. Pan, X. Liu, Broadband microwave absorbing materials based on MWCNTs electromagnetic wave filtering effect, Compos. B Eng. 171 (2019) 214–221, https://doi.org/10.1016/j.compositesb.2019.04.034.

[4] H. Lu, A. Zhang, Y. Zhang, L. Ding, Y. Zheng, The effect of polymer polarity on the microwave absorbing properties of MWNTs, RSC Adv. 5 (2015) 64925–64931, https://doi.org/10.1039/c5ra11528k.

[5] J. Hua, Y. Li, X. Liu, X. Li, S. Lin, J. Gu, Z.K. Cui, Q. Zhuan, Graphene/MWNT/Poly (p-phenylenebenzobisoxazole) multiphase nanocomposite via solution prepolymerization with superior microwave absorption properties and thermal stability, J. Phys. Chem. C 121 (2017) 1072–1081, https://doi.org/10.1021/acs.jpcc.6b11925.

[6] X. Tian, F. Meng, F. Meng, X. Chen, Y. Guo, Y. Wang, W. Zhu, Z. Zhou, Synergistic enhancement of microwave absorption using hybridized polyaniline@helical CNTs with dual chirality, ACS Appl. Mater. Interfaces 9 (2017) 15711–15718, https://doi.org/10.1021/acsami.7b02607.

[7] W. Ma, R. Yang, H. Xie, T. Wang, Facile preparation of aluminum nitridedecorated multi-walled carbon nanotube for excellent microwave absorption, J. Mater. Sci. 56 (2021) 9807–9823, https://doi.org/10.1007/s10853-021-05913-2.

[8] Y. Sun, W. Cui, J. Li, J. Wu, In-situ growth strategy to fabrication of MWCNTs/Fe_3O_4 with controllable interface polarization intensity and wide band electromagnetic absorption performance, J. Alloys Compd. 770 (2019) 67–75, https://doi.org/10.1016/j.jallcom.2018.08.106.

[9] Q. Hu, R. Yang, S. Yang, W. Huang, Z. Zeng, X. Gui, Metal-organic framework-derived core-shell nanospheres anchored on Fe-filled carbon nanotube sponge for strong wideband microwave absorption, ACS Appl. Mater. Interfaces 14 (2022) 10577–10587. https://doi/10.1021/acsami.1c25019.

[10] F. Li, W. Zhan, Y. Su, S.H. Siyal, G. Bai, W. Xiao, A. Zhou, G. Sui, X. Yang, Achieving excellent electromagnetic wave absorption of $ZnFe_2O_4$@CNT/polyvinylidene fluoride flexible composite membranes by adjusting processing conditions, CompositesPart A, Applied Science and Manufacturing 133 (2020) 105866, https://doi.org/10.1016/j.compositesa.2020.105866.

[11] K. Shang, C. Miao, Z. Chen, J. Ouyang, Light-weight FeCo/CNTs/HNTs triple-phase magnetic composites for high-performance microwave absorption, Colloids Surf. A Physicochem. Eng. Asp. 648 (2022) 129121, https://doi.org/10.1016/j.colsurfa.2022.129121.

[12] B. Bateer, X. Wang, C. Tian, Y. Xie, K. Pan, W. Ping, H. Fu, Ni_2P nanocrystals coated on carbon nanotube as enhanced lightweight electromagneticwave absorbers, Carbon 161 (2020) 51–61, https://doi.org/10.1016/j.carbon.2019.12.061.

[13] J. Zhang, R. Shu, C. Guo, R. Sun, Y. Chen, J. Yuan, Fabrication of nickel ferrite microspheres decorated multi-walled carbon nanotubes hybrid composites with enhanced electromagnetic wave absorption properties, J. Alloys Compd. 784 (2019) 422–430, https://doi.org/10.1016/j.jallcom.2019.01.073.

[14] K. Yu, M. Zeng, Y. Yin, X. Zeng, J. Liu, Y. Li, W. Tang, Y. Wang, J. An, J. He, R. Yu, MWCNTs as conductive network for monodispersed Fe_3O_4 nanoparticles to enhance the wave absorption performances, Adv. Eng. Mater. 20 (2018) 1700543.

[15] W. Xia, X. Wang, D. Liu, C. Li, J. Xie, C. Xiong, Enhanced microwave absorbing performance of epoxy composites filled with solvent-free and liquid-like Fe_3O_4 organic hybrid material, Appl. Surf. Sci. 615 (2023) 156376, https://doi.org/10.1016/j.apsusc.2023.156376.

[16] Y. Takagi, Y. Kusunoki, Y. Yoshida, H. Tanaka, G. Saito, K. Katagiri, T. Oshiki, Preparation of magnetic ionic liquids composed of hybrid-type anions, Aust. J. Chem. 65 (2012) 1557, https://doi.org/10.1071/ch12331.

[17] R.E. Del Sesto, T.M. McCleskey, A.K. Burrell, G.A. Baker, J.D. Thompson, B.L. Scott, J.S. Wilke, P. Williams, Structure and magnetic behavior of transition metal based ionic liquids, Chem. Commun. 4 (2008) 447–449, https://doi.org/10.1039/b711189d.

[18] R.R. Henriques, C.P. Oliveira, R. Stein, K. Pontes, A.A. Silva, B.G. Soares, Dual role of magnetic ionic liquids as curing agents of epoxy resin and microwave-absorbing additives, ACS Appl. Polym. Mater. 4 (2022) 1207–1217, https://doi.org/10.1021/acsapm.1c01584.

[19] T. Fukushima, A. Kosaka, Y. Ishimura, T. Yamamoto, T. Takigawa, N. Ishii, T. Aida, Molecular ordering of organic molten salts triggered by single-walled carbon nanotubes, Science 300 (2003) 2072–2074, https://doi.org/10.1126/science.1082289.

[20] J.B. Ducros, N. Buchtova, A. Magrez, O. Chauvet, J. Le Bideau, Ionic and electronic conductivities in carbon nanotubes–ionogel solid device, J. Mater. Chem. 21 (2011) 2508–2511, https://doi.org/10.1039/c0jm02016h.

[21] J. Gong, F. Yang, Q. Shao, X. He, X. Zhang, S. Liu, L. Tang, Y. Deng, Microwave absorption performance of methylimidazolium ionic liquids: towards novel ultra-wideband metamaterial absorbers, RSC Adv. 7 (2017) 41980–41988, https://doi.org/10.1039/C7RA06709G.

[22] F. Yang, J. Gong, E. Yang, Y. Guan, X. He, S. Liu, X. Zhang, Y. Deng, Ultra broadband metamaterial absorbers based on ionic liquids, Appl. Phys. A 125 (2019) 149, https://doi.org/10.1007/s00339-019-2443-x.

[23] M. Mohamadi, E. Kowsari, M. Yousefzadeh, A. Chinnappan, S. Ramakrishna, Highly-efficient microwave absorptivity in reduced graphene oxide modified with PTA@imidazolium based dicationic ionic liquid and fluorine atom, Compos. Sci. Technol. 188 (2020) 107960, https://doi.org/10.1016/j.compscitech.2019.107960.

[24] E. Kowsari, M. Mohammadi, Synthesis of reduced and functional grapheneoxide with magnetic ionic liquid and its application as an electromagnetic-absorbing coating, Compos. Sci. Technol. 126 (2016) 106–114, https://doi.org/10.1016/j.compscitech.2016.02.019.

[25] H. Wei, S. Chen, Z. Chen, L. Tang, J. Xue, C. Wang, Z. Wang, Y. Li, Hetero–interface engineering of biomass carbon foam for broadband microwave absorption and thermal insulation properties, Carbon 241 (2025) 120382, https://doi.org/10.1016/j.carbon.2025.120385.

[26] Y. Li, S. Guo, L. Zhao, S. Chen, Y. Li, X. Yang, P. Wang, W. Feng, Z. Mou, H. Jiang, H. Wei, G. Cerullo, Controlled preparation of lightweight,resilient helical carbon fibers for high-performance microwave absorption and oil-water separation, Carbon 233 (2025) 119923, https://doi.org/10.1016/j.carbon.2024.119923.

[27] S. Chen, Z. Chen, L. Tang, J. Xue, Z. Wang, Y. Li, H. Wei, Nitrogen-doped porous biomass-derived carbons for enhanced hydrophobicity, microwave absorption and thermal insulation, Fuel 406 (2026) 136936, https://doi.org/10.1016/j.fuel.2025.136936.

[28] N. Sun, X. Gao, A. Wu, F. Lu, L. Zheng, Mechanically strong ionogels formed by immobilizing ionic liquid in polyzwitterion networks, J. Mol. Liq. 248 (2017) 759–766, https://doi.org/10.1016/j.molliq.2017.10.121.

[29] H. Song, X. Yu, D.H. Nguyen, C. Zhang, T. Liu, Highly stretchable, self-healable and self-adhesive polyzwitterion ionogels enabled with binary noncovalent interactions, Compos. Commun. 34 (2022) 101251, https://doi.org/10.1016/j.coco.2022.101251.

[30] C. Li, S. Zhang, X. Wang, M. Xu, C. Xiong, Q. Yang, Efficient and thinmicrowave absorption materials fabricated by polyzwitterion wrapped carbon nanotube, Appl. Surf. Sci. 600 (2022) 154060, https://doi.org/10.1016/j.apsusc.2022.154060.

[31] Y. Leng, P. Jiang, J. Wang, A novel Brønsted acidic heteropolyanion-basedpolymeric hybrid catalyst for esterification, Catal. Commun. 25 (2012) 41–44, https://doi.org/10.1016/j.catcom.2012.04.014.

[32] D. Li, J. Li, D. Mao, H. Wen, Y. Zhou, J. Wang, Direct synthesis of sulfonic group tethered mesoporous poly(ionic liquid) for catalyzing deoximation reactions, Mater. Chem. Phys. 189 (2017) 118–126, https://doi.org/10.1016/j.matchemphys.2016.12.067.

[33] X. Yu, X. Yuan, Y. Zhao, L. Ren, From paramagnetic to superparamagnetic ionic Liquid/Poly(ionic liquid): the effect of pi-pi stacking interaction, ACS Macro Lett. 8 (2019) 1504–1510, https://doi.org/10.1021/acsmacrolett.9b00714.

[34] C. Ding, W. Xia, S. Zhang, C. Li, X. Liao, M. Liu, J. Chen, Y. Yu, S. Qin, C. Xiong, Tunable and efficient electromagnetic wave absorption of carbon material modulating magnetic ionic polymer-based composites, Colloids Surf. A Physicochem. Eng. Asp. 676 (2023) 132207, https://doi.org/10.1016/j.colsurfa.2023.132207.

[35] N. Calisi, S. Martinuzzi, A. Giaccherini, C.S. Pomelli, L. Guazzelli, S. Caporali, Temperature and angle resolved XPS study of BMImCl and BMIm $FeCl_4$, J. Electron. Spectrosc. Relat. Phenom. 247 (2021) 147034, https://doi.org/10.1016/j.elspec.2020.147034.

[36] T. Okubo, R. Kawajiri, T. Mitani, T. Shimoda, A Mixed-Valence Coordination Polymer Featuring Two-Dimensional Ferroelectric Order: {$[CuI_4CuII(Et_2dtc)_2Cl_3][CuII(Et_2dtc)_2]_2(FeCl_4)$}n($Et_2$dtc=diethyldithiocarbamate), J. Am. Chem. Soc. 127 (50) (2005) 17598–17599. https://pubs.acs.org/doi/full/10.1021/ja056030p/.

[37] E.E. El-Katori, M.I. Nessim, M.A. Deyab, K. Shalabi, Electrochemical, XPS and theoretical examination on the corrosion inhibition efficacy of stainless steel via novel imidazolium ionic liquids in acidic solution, J. Mol. Liq. 337 (2021) 116467, https://doi.org/10.1016/j.molliq.2021.116467.

[38] G. Duan, Y. Wang, B. Luo, L. Sun, S.J. Zheng, J. Huang, Z. Ye, Taurine-Mediated dynamic bridging strategy for highly stable Zn metal anode, Energy Storage Mater. 61 (2023) 102882, https://doi.org/10.1016/j.ensm.2023.102882.

[39] L. Wu, H. Yuan, Y. An, J. Sun, Y. Liu, H. Tang, W. Yang, L. Cui, J. Li, Q. An, Sulfurized composite interphase enables a highly reversible Zn anode, Angew. Chem. Int. Ed. (2025) e202419495, https://doi.org/10.1002/anie.202419495.

[40] M. Wei, L. Wang, S.U. Rehman, X. Luo, Y. Hu, C. Chen, T. Liang, SiC@Co-CNT composites with tunable electromagnetic parameters for microwave absorption, J. Alloys Compd. 1010 (2025) 177633, https://doi.org/10.1016/j.jallcom.2024.177663.

[41] S. Lu, Y. Meng, H. Wang, F. Wang, J. Yuan, H. Chen, Y. Dai, J. Chen, Great enhancement of electromagnetic wave absorption of MWCNTs@carbonaceous CoO composites derived from MWCNTs-interconnected zeolitic imidazole framework, Appl. Surf. Sci. 481 (2019) 99–107, https://doi.org/10.1016/j.apsusc.2019.03.018.

[42] X. Liu, L. Yu, G. Zhu, Z. Wang, G. Lian, X. Xiong, W. You, R. Che, Hollow porous FeCo/Cu/CNTs composite microspheres with excellent microwave absorption performance, Nano Res. 17 (11) (2024) 9857–9864, https://doi.org/10.1007/s12274-024-6963-0.

[43] Y.Y. Wang, W.J. Sun, K. Dai, D.X. Yan, Z.M. Li, Highly enhanced microwave absorption for carbon nanotube/barium ferrite composite with ultra-low carbon nanotube loading, J. Mater. Sci. Technol. 102 (2022) 115–122, https://doi.org/10.1016/j.jmst.2021.06.032.

[44] Y.M. Li, Y.R. Li, H.P. Fang, Y. Deng, D.Y. Wang, Optimization design of the multidimensional heterostructure toward lightweight, broadband, highly efficient, and flame-retarding electromagnetic wave-absorbing composites, ACS Appl. Mater. Interfaces 38 (2024) 51333–51345, https://doi.org/10.1021/acsami.4c10557.

[45] M. Wei, L. Wang, S.U. Rehman, X. Luo, Y. Hu, C. Chen, T. Liang, Synthesis and electromagnetic wave absorption properties of 3D spherical $NiCo_2S_4$ composites, J. Alloys Compd. 795 (2019) 327–335, https://doi.org/10.1016/j.jallcom.2019.04.336.

[46] G. Chen, R. Liu, D. Feng, Facile synthesis of cross-linked network structure $CoNiZnFe_2O_4$@CNT composite with excellent microwave absorption performance, Ceram. Int. 51 (2025) 22431–22444, https://doi.org/10.1016/j.ceramint.2025.03.244.

[47] Y. Yang, X. Liu, J. Zhao, X. Jia, Z. Li, C. Xiao, J. Wang, Y. Li, J. Liang, S. Ding, W. Yu, Confined dissipation cage in dual-shell structured Ti_3C_2Tx@CNTs/Ni hollow spheres for lightweight and broadband electromagnetic wave absorption, Chem. Eng. J. 473 (2023) 145250, https://doi.org/10.1016/j.cej.2023.145250.

[48] J. Weng, Y. Liu, X. Huang, Synthesis of in situ grown CNTs on MOF-derived Ni@CNT with tailorable microstructures toward regulation of electromagnetic wave absorption performance, Carbon 231 (2025) 119678, https://doi.org/10.1016/j.carbon.2024.119678.

[49] Z. Jia, C. Wang, A. Feng, P. Shi, C. Zhang, X. Liu, K. Wang, G. Wu, A low-dielectric decoration strategy to achieve absorption-dominated electromagnetic shielding material, Compos. B Eng. 183 (2020) 107690, https://doi.org/10.1016/j.compositesb.2019.107690.

[50] P. Liu, S. Gao, Y. Wang, F. Zhou, Y. Huang, J. Luo, Metal-organic polymer coordination materials derived Co/N-doped porous carbon composites for frequency-selective microwave absorption, Compos. B Eng. 202 (2020) 108406, https://doi.org/10.1016/j.compositesb.2020.108406.

[51] N. Qu, G. Xu, Y. Liu, M. He, R. Xing, J. Gu, J. Kong, Multi-scale design of metal–organic framework metamaterials for broad-band microwave absorption, Adv. Funct. Mater. 35 (2025) 2402923, https://doi.org/10.1002/adfm.202402923.

[52] X. Rong, F. Xin, H. Chen, Z. Ke J. Tao, L. Wang, Defect engineering on carbon nanotubes or graphene to balance conduction and polarization loss for enhancing microwave absorption, ACS Appl. Nano Mater. 8 (2025) 813–827, https://doi.org/10.1021/acsanm.4c06217.

[53] J. Liu, S. Zhang, D. Qu, X. Zhou, M. Yin, C. Wang, X. Zhang, S. Li, P. Zhang, Y. Zhou, K. Tao, M. Li, B. Wei, H. Wu, Defects-Rich heterostructures trigger strong polarization coupling in Sulfdes/Carbon composites with robust electromagnetic wave absorption, Nano-Micro Lett. 17 (2024) 24, https://doi.org/10.1007/s40820-024-01515-0.

[54] J. Xu, B. Li, Z. Ma, X. Zhang, C. Zhu, F. Yan, P. Yang, Y. Chen, Multifunctional film assembled from N-Doped carbon nanofiber with Co–N_4–O single atoms for highly efficient electromagnetic energy attenuation, Nano-Micro Lett. 16 (2024) 240, https://doi.org/10.1007/s40820-024-01440-2.

[55] J. Mei, J. Luo, T. Zhao, S. Jiang, Y. Wu, Z. Dai, Y. Xie, Morphology engineering of MIL-88A-derived 0D/1D/2D nanocomposites toward wideband microwave absorption, J. Mater. Sci. Technol. 226 (2025) 65–75, https://doi.org/10.1016/j.jmst.2024.12.012.

[56] Y. Chen, J. Luo, C. Xue, Z. Huang, M. He, X. Liu, Y. Xie, Self-assembled nanostructures of 0D ZnO on 3D chitin-derived carbon aerogel for wideband electromagnetic wave absorption, Carbon 226 (2025) 120382, https://doi.org/10.1016/j.jmst.2025.03.028.

[57] F. Yang, J. Gong, E. Yang, Y. Guan, X. He, S. Liu, X. Zhang, Y. Deng, Microwave-absorbing properties of room-temperature ionic liquids, J. Phys. Appl. Phys. 52 (2019) 155302, https://doi.org/10.1088/1361-6463/ab016c.

[58] M. Tang, Y. Shen, Poly(ionic liquid)s as optically transparent microwave-absorbing materials, Macromolecules 41 (2007) 493–496, https://doi.org/10.1021/ma071762i.

[59] X. Wang, J. Luo, S. Mao, D. Cheng, X. Liu, Y. Xie, L. Cheng, Electromagnetic collaborative optimization of DyFe-MOFs derivatives for ultra-thin electromagnetic wave absorption, J. Adv. Ceram. 14 (2025) 9221163, https://doi.org/10.26599/JAC.2025.9221163.

[60] Q. Wang, J. Luo, Y. Wu, Y. Xie, L. Cheng, Tunable electromagnetic response behaviors via cross-scale morphological structural engineering for ultra-wideband microwave absorption, Chin. J. Chem. 43 (2025) 2756–2770, https://doi.org/10.1002/cjoc.70169.

[61] W. Zhang, J. Luo, J. Shi, B. Han, X. Li, Y. Xie, Conductive MOFs with tailored polarization loss for broadband absorption at ultrathin thickness, Nano Res. 18 (2025) 94907919, https://doi.org/10.26599/NR.2025.94907919.

[62] Z. Sun, J. Luo, H. Zhao, Y. Wu, X. Liu, Y. Xie, Multi-dimensional Sb_2S_3@MoS_2 heterojunctions for electromagnetic wave absorption, Mater. Today Nano 30 (2025) 100620, https://doi.org/10.1016/j.mtnano.2025.100620.

[63] X. Liu, Q. Wang, P. Shu, Y. Wu, X. Li, J. Luo, Multicomponent competitive synergistically active $NiFe_2O_4$/C-g-C_3N_4/RGO heterostructure for efficientelectromagnetic wave absorption, Carbon 234 (2025) 119964, https://doi.org/10.1016/j.carbon.2024.119964.

[64] J. Zhang, M. Niu, Z. Zhang, L. Chen, R. Sun, Z. Zhang, X. Wang, The polarization loss induced by interfacial charge redistribution using Ar plasma treatment in Ni@C composites for superior microwave absorption performance, Chem. Eng. J. 507 (2025) 160489, https://doi.org/10.1016/j.cej.2025.160489.